

Strong confinement of active microalgae leads to inversion of vortex flow and enhanced transport

Debasmita Mondal,¹ Ameya G. Prabhune,^{1,2} Sriram Ramaswamy,³ and Prerna Sharma^{1,*}

¹*Department of Physics, Indian Institute of Science,
Bangalore, Karnataka 560012, India*

²*Department of Physics, University of Colorado Boulder, Boulder, Colorado 80309, USA.*

³*Centre for Condensed Matter Theory,
Department of Physics, Indian Institute of Science,
Bangalore, Karnataka 560012, India*

Abstract

Active microorganisms, swimming through viscous fluids, imprint their propulsion mechanisms in the generated flow fields. Extreme confinement of these swimmers between rigid boundaries often arises in natural and technological contexts, yet measurements of their mechanics in this regime are absent. Here, we show that strongly confining the microalga *Chlamydomonas* between two parallel plates not only inhibits its motility but also leads, for purely mechanical reasons, to inversion of the surrounding vortex flows. This contrasts with expectations based on the source-dipole description of confined swimmers. Insights from the experiment lead to a simplified theoretical description of flow fields based on a quasi-2D Brinkman approximation to the Stokes equation than the usual method of images. We argue that this vortex flow inversion provides the advantage of enhanced nutrient transport to the organism despite higher friction. Overall, our results offer a comprehensive framework for analyzing the collective flows of strongly confined swimmers.

* prerna@iisc.ac.in

INTRODUCTION

Fluid friction governs the functional and mechanical responses of microorganisms which operate at low Reynolds number. They have exploited this friction and developed drag-based propulsive strategies to swim through viscous fluids [1, 2]. Naturally, many studies have elucidated aspects of the motility and flow fields of microswimmers in a variety of settings that mimic their natural habitats [3–6]. The self-propulsion of microbes in crowded and strongly confined environments is one such setting, encountered very commonly in the natural world as well as in controlled laboratory experiments. Examples include microbial biofilms, bacteria- and algae-laden porous rocks or soil [6–9]; parasitic infections in crowded blood streams and tissues [10]; and biomechanics experiments using thin films and microfluidic channels [5, 11–14]. Confined microswimmers are also fundamentally interesting as active suspensions [15, 16] and there are efforts to mimic these by chemical and mechanical means for applications in nano- and microtechnologies [17, 18].

The mechanical interaction of microswimmers with confining boundaries alters their motility and flow fields [1, 15, 19], leading to emergent self-organization in cell-cell coordination [20, 21], spatial distribution of cells [22, 23], and ecological aspects such as energy expenditure, nutrient uptake, fluid mixing, transport and sensing [24, 25]. It is expected that steric interactions will dominate with increasing confinement at the swimmer-wall interface and that hydrodynamic screening by the confining wall will lead to recirculating flow patterns or vortices [19, 26].

Among the abundant diversity of microswimmers, the unicellular and biflagellated algae *Chlamydomonas reinhardtii* (CR), with body diameter $D \approx 10 \mu\text{m}$, are a versatile model system, widely used for understanding cellular processes such as carbon fixation, DNA repair and damage, phototaxis, ciliary beating [27–30] and physical phenomena of biological fluid dynamics [31–33]. They are considered next-generation resources for wastewater remediation and synthesis of biofuel, biocatalysts, and pharmaceuticals [8, 34]. Recently, extreme confinement between two hard walls has been exploited to stress prime CR cells towards enhanced biomass production and cell viability [35, 36]. Despite the existing and emerging contexts outlined above, knowledge about how rigid walls might modify the kinetics, kinematics, ecological characteristics and theoretical description of a strongly confined microalga such as CR (or any other microswimmer) is scarce. All studies prior to ours have exclusively focused on the effect of boundaries on CR dynamics in *soft* PDMS chambers or thin fluid

films of height $H \gtrsim 14 \mu\text{m}$ [12, 13, 37], i.e., for weak confinement, $D/H < 1$.

Here, we present the first experimental measurements of the flagellar waveform, motility and flow fields of *strongly confined* CR cells placed in between two *hard* glass walls $\sim 10 \mu\text{m}$ apart ($D/H \gtrsim 1$, denoted ‘H10 cells’), and infer from them the effect of confinement on kinetics, energy dissipation, nutrient transport and fluid mixing due to the cells. We also measure the corresponding quantities for weakly confined cells placed in glass chambers of height $H = 30 \mu\text{m}$ ($D/H \sim 0.3$, denoted ‘H30 cells’) for comparison. We find that the cell speed decreases significantly and the trajectory tortuosity increases with increasing confinement as we go from H30 to H10 cells.

Most surprisingly, the beat-cycle averaged experimental flow field of strongly confined cells has opposite flow vorticity, not only to that expected from the screened version of bulk flow [37, 38], but also to those predicted from the source dipole theory of strongly confined swimmers [15, 19]. We attribute this counterintuitive result to the negligible cell drag as compared to the flagellar thrust by calculating the forces acting on the cell. This results in a 38% increase in the volumetric flow rate towards the H10 cells as compared to H30 cells which suggests that flagella-generated flows enhance the mass transport of nutrients to the slow-moving H10 cell surface, despite higher drag due to the strongly confining walls. We complement our experimental results with a simple theoretical description of the strongly confined microswimmer flows using a quasi-2D steady Brinkman approximation to the Stokes equation [39], instead of the complicated method of recursive images [19, 40]. Solving this equation, we demonstrate that the vortex flow inversion in strong confinement is well-described as arising from a pair of like-signed force densities localized with a Gaussian spread around the approximate flagellar positions rather than the conventional three overall neutral point forces for CR [38]. Force balance enables us to quantitatively measure the substrate friction experienced by the H10 cells.

RESULTS

Experimental System

Synchronously grown wild-type CR cells (strain CC 1690) swim in a fluid medium using the characteristic breaststroke motion of two $\sim 11 \mu\text{m}$ long anterior flagella with beat frequency $\nu_b \sim 50 - 60 \text{ Hz}$. These cells are introduced into rectangular quasi-2D chambers (area, 18

mm \times 6 mm) made up of a glass slide and coverslip sandwich with double tape of thickness $H = 10/30 \mu\text{m}$ as spacer. Passive 200 nm latex microspheres are added as tracers to the cell suspension for measuring the fluid flow using particle-tracking velocimetry (PTV). We use high-speed phase-contrast imaging at ~ 500 frames/second and 40X magnification to capture flagellar waveform and cellular and tracer motion at a distance $H/2$ from the solid walls. The detailed experimental procedure is described in the Materials and Methods section.

Mechanical equilibrium of confined cells

The net force and torque on a neutrally buoyant microswimmer such as CR, together with the ambient medium and boundaries, are zero [2, 3, 19, 32]. The two local forces exerted by any dipolar microswimmer on the surrounding fluid are flagellar propulsive thrust \mathbf{F}_{th} and cell body drag \mathbf{F}_{cd} . They balance each other completely for any swimmer in an unbounded medium [1, 31] and approximately in weak confinement between two hard walls (Figure 1A). In these regimes, CR is the classic example of an active puller where the direction of force dipole due to thrust and drag are such that the cell draws in fluid along the propulsion axis (x -axis in Figure 1A) and ejects it in the perpendicular plane [1]. CR is described well by three point forces or Stokeslets [38] as in Figure 1A because the thrust is spatially extended and distributed equally between the two flagella. However, microswimmers in strong confinement between two closely spaced hard walls, $D/H \gtrsim 1$, are in a regime altogether different from bulk because the close proximity of the cells to the glass walls results in an additional drag force \mathbf{F}_{wd} (Figure 1B). Therefore, the flagellar thrust is balanced by the combined drag due to the cell body and the strongly confining walls (Figure 1B).

Size polydispersity, confinement heterogeneity, and consequences for flagellar waveform and motility

We define the degree of confinement of the CR cells as the ratio D/H of cell body diameter to chamber height. CR cells in chambers of height $H = 30 \mu\text{m}$ are always in weak confinement as the cell diameter varies within $D \sim 8 - 14 \mu\text{m} < H$. However, this dispersity in cell size becomes significant when CR cells are swimming within quasi-2D chambers of height, $H = 10 \mu\text{m}$. Here, the diameter of individual cells is crucial in determining the

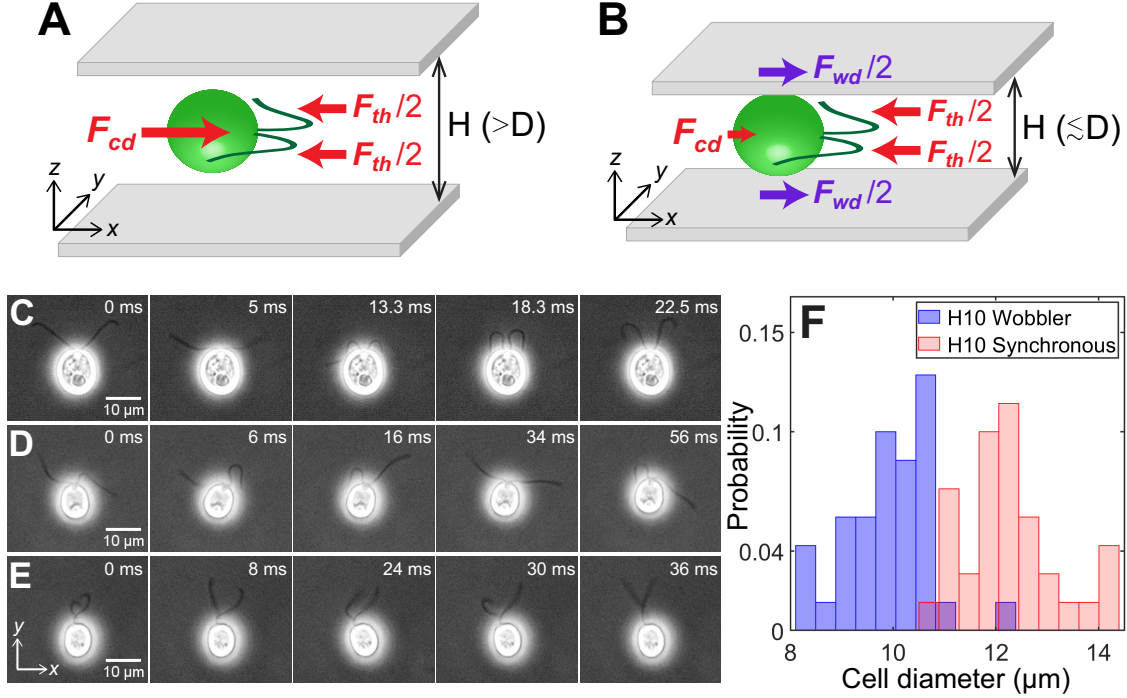


Figure 1. Cell size affects forces acting on confined microswimmers. Schematics of the forces exerted by a *Chlamydomonas* cell (green) swimming along the x -axis in between two glass plates separated by height, H under (A) weak confinement where the cell's body diameter, $D < H$ and (B) strong confinement where $D \gtrsim H$. Solid arrows represent local forces exerted by the cell on the surrounding medium. F_{th} and F_{cd} are the propulsive thrust distributed equally between the two flagella and Stokes drag due to the cell body, respectively. F_{wd} is wall friction force for the strongly confined cell body in contact with both the walls (B). Time lapse images of CR cells swimming in a quasi-2D chamber of height $H = 10 \mu\text{m}$ with (C) synchronously beating flagella with $\nu_b \sim 39 \text{ Hz}$ ($D \sim 13.2 \mu\text{m}$); (D) asynchronously beating flagella ($D \sim 9.9 \mu\text{m}$); and (E) paddler type flagellar beat ($D \sim 9.7 \mu\text{m}$). The cell bodies in (D) and (E) wobble due to their irregular flagellar beat pattern and are called 'Wobblers'. (F) Histogram of cell body diameter in the chamber of $H = 10 \mu\text{m}$ (Number of cells, $n = 70$). Synchronously beating cells ($n = 34$) typically have larger diameter than Wobblers ($n = 36$) and thus the H10 Synchronous cells with $D/H \gtrsim 1$ are strongly confined.

character – weak or strong – of the confinement and, as a consequence, the forces acting on the cell. Below, we illustrate how the cell size determines the type of confinement in this regime through measurements of flagellar waveform and cell motility.

CR cells confined to swim in $H = 10 \mu\text{m}$ chambers show three kinds of flagellar waveform:

(a) synchronous breaststroke and planar beating of flagella interrupted by intermittent phase slips ('H10 Synchronous', Figure 1C, Video 1); (b) asynchronous and planar flagellar beat over large time periods (Figure 1D, Video 2); and (c) a distinctive paddling flagellar beat wherein flagella often wind around each other and paddle irregularly anterior to the cell with their beat plane oriented away from the $x - y$ plane. (Figure 1E, Video 2). While both synchronous and asynchronous beats are typically observed for CR in bulk [41] and weak confinement of $30 \mu\text{m}$ chamber height, the paddler beat is not observed in either of these conditions. The cell body wobbles for both asynchronous and paddler beat of cells (Figure 1D & E) and often the flagellar waveform in a single CR switches between these two kinds (Video 2). Hence, we collectively call them 'H10 Wobblers' [42].

We correlate the Synchronous and Wobbler nature of cells to their body diameter (Figure 1F). The mean projected diameter in the image plane of Synchronous cells ($D = 12.28 \pm 0.94 \mu\text{m}$, Number of cells, $n = 34$) is larger than that of Wobblers ($D = 9.92 \pm 0.85 \mu\text{m}$, $n = 36$). Hence, the former's cell body is squashed and *strongly confined* in $H = 10 \mu\text{m}$

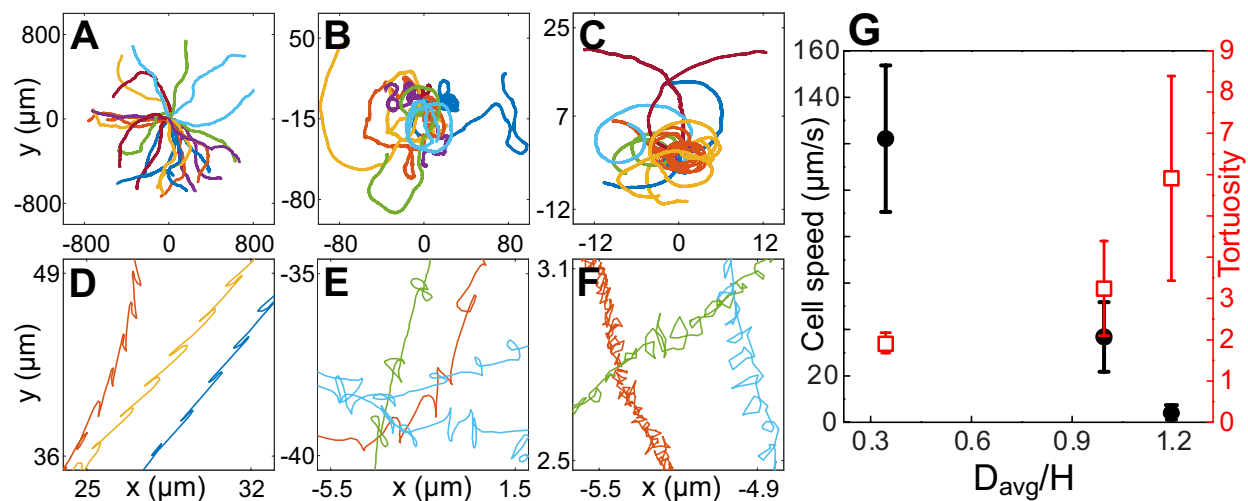


Figure 2. Cell motility in confinement. Representative trajectories of CR cells in (A) $H = 30 \mu\text{m}$ ($n = 25$), (B) $H = 10 \mu\text{m}$, Wobblers ($n = 13$); (C) $H = 10 \mu\text{m}$ ($n = 17$), Synchronous cells. All of these trajectories lasted for 8.2 s and their initial positions are shifted to origin. (D), (E) and (F) are the zoomed in trajectories of (A), (B) and (C), respectively. (G) Cell speed (circles) and tortuosity of trajectories (squares) as a function of the degree of confinement (D_{avg}/H), D_{avg} being the average body diameter of a population of cells ($n = 52, 36, 23$ for H30, H10 Wobbler and H10 Synchronous, respectively). The errorbar in the plot corresponds to standard deviation of the data.

chamber in comparison with that of the latter. This leads to planar swimming of Synchronous cells, whereas Wobblers tend to trace out a near-helical trajectory which is a remnant of its behaviour in the bulk. Thus, the Wobblers likely compromise their flagellar beat into asynchrony and/or paddling over long periods due to frequent interactions with the solid boundaries while rolling and yawing their cell body [29].

The motility of CR cells in $H = 30 \mu\text{m}$ is similar to that in bulk and has the signature of back-and-forth cellular motion due to the recovery and power strokes of the flagella (Figure 2A,D). As confinement increases, the drag on the cells due to the solid walls increases and they trace out smaller distances with increasing twists and turns in the trajectory (Figure 2A-F). These phenomena can be quantitatively characterized by cell speed and trajectory tortuosity (Materials and Methods) as a function of the degree of confinement of the cells (Figure 2G). Cellular speed decreases and tortuosity of trajectories increases with increasing confinement as we go from H30 \rightarrow H10 Wobblers \rightarrow H10 Synchronous cells. Notably, the cell speed u decreases by 96% from H30 ($\langle u^{30} \rangle = 122.14 \pm 31.59 \mu\text{m/s}$, $n = 52$) to H10 Synchronous swimmers ($\langle u^{10} \rangle = 4.07 \pm 2.88 \mu\text{m/s}$, $n = 23$). Henceforth, we equivalently refer to the H10 Synchronous CR as ‘*strongly confined*’ or ‘*H10*’ cells ($D/H \gtrsim 1$) and the H30 cells as ‘*weakly confined*’ ($D/H < 1$).

Experimental flow fields

We measure the beat-averaged flow fields of H30 and H10 CR cells to systematically understand the effect of strong confinement on the swimmer’s flow field. We determine the flow field for H30 cells only when their flagellar beat is in the $x - y$ plane (Video 3) for appropriate comparison with planar H10 swimmers. Figure 3A shows the velocity field for H30 cells obtained by averaging ~ 178 beat cycles from 32 cells. It shows standard features of an unbounded CR’s flow field [37, 38] namely, far-field 4-lobe flow of a puller, two lateral vortices at 8-9 μm from cell’s major axis and anterior flow along the swimming direction till a stagnation point, 21 μm from the cell centre (Figure 3B). These near-field flow characteristics are quite well explained theoretically by a 3-bead model [43–45] or a 3-Stokeslet model [38], where the thrust is distributed at approximate flagellar positions between two Stokeslets of strength $(-1/2, -1/2)$ balanced by a $+1$ Stokeslet due to viscous drag on the cell body (Figure 1A).

The flow field of a representative H10 swimmer ($u = 5.67 \pm 1.57 \mu\text{m/s}$, $\nu_b \sim 40 \text{ Hz}$) is

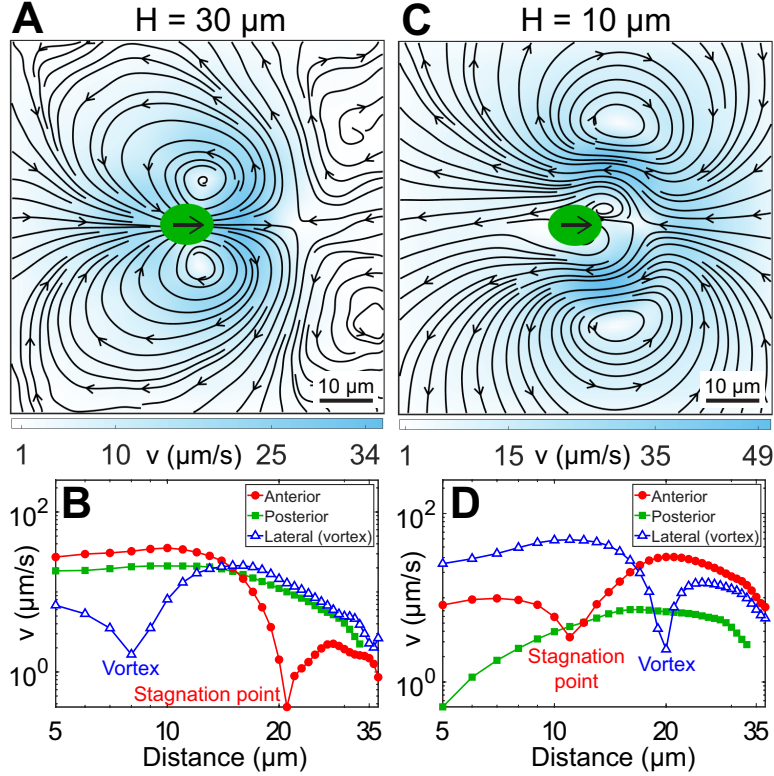


Figure 3. Experimental flow fields of CR cells in weak and strong confinement. Experimentally measured, beat-averaged flow fields in the $x - y$ plane of synchronously beating CR cells swimming in (A) $H = 30 \mu\text{m}$, (C) $H = 10 \mu\text{m}$. Black arrows on the cell body indicate that the cells are swimming to the right. Solid black lines indicate the streamlines of the flow in lab frame. The colorbars represent flow magnitude, v . (B) and (D) denote the speed variation in (A) and (C), respectively, along anterior, posterior and lateral to the cell (where the vortices are present). Distances along anterior and posterior are measured along horizontal lines from the cell centre $(0, 0)$; whereas the lateral (vortex) distances are measured along the vertical line passing through $(x, y) = (2, 0)$ for (B) and $(8, 0)$ for (D), respectively.

Figure supplement 1. Expected flow fields of a strongly confined CR using conventional theoretical approaches.

shown in Figure 3C, averaged over ~ 328 beat cycles. Strikingly, the vortices contributing dominantly to the flow in this strongly confined geometry are opposite in sign to those in the bulk [38] or weakly confined case ($H=30$, Figure 3A). This 2-lobed flow is quite distinct from expectations based on the screened version of the bulk or 3-Stokeslet flow, which is 4-lobed (Figure 3—figure supplement 1A). More surprisingly, this inverse vortical flow is in stark contrast to the theoretical prediction that the far-field flow of a confined microswimmer is that

of 2D source dipole pointing along the swimming direction (Figure 3—figure supplement 1B) [12, 15, 19]. On the contrary, the far-field looks more like a source dipole pointing opposite to the swimmer’s motion. Other significant differences from the bulk flow include front-back flow asymmetry, opposite flow direction posterior to the cell, distant lateral vortices (20 μm) and closer stagnation point (11 μm) (Figure 3D). All other H10 Synchronous swimmers, including the slowest ($u \sim 0.15 \mu\text{m/s}$) and the fastest ($u \sim 14 \mu\text{m/s}$) cells, show similar flow features. Even though the flow fields of H30 and H10 cells look strikingly different, the viscous power dissipated through the flow fields is nearly same (Appendix 1.1).

A close examination suggests that the vortex contents of the flow fields of Figures 3A (H30) and 3C (H10) are mutually compatible. The large vortices flanking the rapidly moving CR in H30 are shrunken and localized close to the cell body in H10 due to the greatly reduced swimming speed. The frontal vortices generated by flagellar motion now fill most of the flow field in H10. Generated largely during the power stroke of flagella, they are opposite in sense to the vortices produced by the moving cell body.

Force balance on confined cells

The forces exerted by the cell on the surrounding medium are described at coarse-grained scales by the Stokeslets \mathbf{F}_{th} , \mathbf{F}_{cd} and \mathbf{F}_{wd} as depicted in Figure 1A,B. Among these three forces, we know $|\mathbf{F}_{cd}| = 3\pi\eta Du$ from the Stokes drag due to a near-spherical cell body of diameter $D \sim 10 \mu\text{m}$ moving at speed u through a fluid of viscosity $\eta = 1 \text{ mPa}\cdot\text{s}$ [31]. This cell-body drag in the regime of weak confinement (H30) is $\mathbf{F}_{cd}^{30} \approx 11.31 \text{ pN } \hat{\mathbf{x}}$ due to the mean cell speed of $u^{30} \approx 120 \mu\text{m/s}$. Using force balance on the fluid element enclosing the weakly confined CR, $\mathbf{F}_{th}^{30} + \mathbf{F}_{cd}^{30} = 0$ (Figure 1A), the flagellar thrust force required to drag the cell body at speed u^{30} is $\mathbf{F}_{th}^{30} \approx -11.31 \text{ pN } \hat{\mathbf{x}}$.

Given that CR operates at nearly constant thrust since $u \propto \eta^{-1}$ [33, 42] and that the flagella of the H10 cell are beating far from the walls ($\sim 5 \mu\text{m}$) with amplitude and waveform similar to that of the H30 cell (Video 1 and 3), we infer the flagellar thrust force in strong confinement to be $\mathbf{F}_{th}^{10} \approx \mathbf{F}_{th}^{30} \approx -11.31 \text{ pN } \hat{\mathbf{x}}$. We also know the Stokes drag due to the strongly confined cell body moving at speed $u^{10} \approx 4 \mu\text{m/s}$ is $\mathbf{F}_{cd}^{10} \approx 0.38 \text{ pN } \hat{\mathbf{x}}$. This is simply the hydrodynamic drag contributed by the cell body at its steadily swimming speed of u^{10} , and does not include the drag due to the strongly confining walls. $|\mathbf{F}_{th}^{10}| \gg |\mathbf{F}_{cd}^{10}|$ confirms that viscous drag due to the cell body alone is negligible compared to the flagellar

propulsive thrust in strong confinement. This force imbalance drives the vortex flow inversion observed in Figure 3C, as will be shown later theoretically, and is further used to calculate the unknown frictional drag due to the walls, \mathbf{F}_{wd} . Force balance on the fluid element and rigid walls enclosing the CR in strong confinement requires $\mathbf{F}_{th}^{10} + \mathbf{F}_{cd}^{10} + \mathbf{F}_{wd}^{10} = 0$ (Figure 1B), which results in $\mathbf{F}_{wd}^{10} \approx 10.93 \text{ pN } \hat{\mathbf{x}}$. Therefore, the flagellar thrust is mostly working against the wall friction as expected due to the extremely low speed of the strongly confined swimmer. This wall drag could in principle originate in direct frictional contact between the cell body and the wall [26] with bonds with a finite or infinite lifetime in the absence of applied shear, or in lubrication, i.e., viscous shear flow in the thin layer of fluid between cell and wall [15, 26]. However, a simple estimate (Appendix 1.2) suggests that lubrication cannot account for the observed drag due to the solid walls.

Enhancement of fluid transport in strong confinement

The photosynthetic alga CR feeds on dissolved inorganic ions/molecules such as phosphate, ammonium, and carbon dioxide in addition to sunlight which is the major source of energy [46, 47]. Optimized nutrient uptake is one of the major traits of a microswimmer [48]. For example, CR flagella adhere to substrates in optimum light conditions for increasing photosynthetic efficiency [49] and their breastroke is more uptake-efficient than an undulatory stroke [46]. Apart from these mechanisms, it is widely known that flagella-generated flow fields can increase the influx of dissolved solute molecules to osmotrophs like CR when the Péclet number is greater than one [27, 31, 46–48, 50].

The flow based Péclet number is defined as $Pe = Vl_V/D_S$ where V and l_V are the diameter and flow-speed of the flagellar vortex and D_S is the solute diffusivity in water [51]. This definition is more appropriate than a Péclet number based on the swimmer’s speed for describing the enhancement of mass transport of solutes due to the vortical flow fields generated by the flagella, particularly for the strongly confined cell (Appendix 1.3). Using the experimentally measured flow data from Figure 3 and $D_S \approx 10^{-9} \text{ m}^2/\text{s}$ [46, 47, 51], we calculate the Péclet numbers for the weakly and strongly confined cell to be $Pe^{30} \approx 0.5$ and $Pe^{10} \approx 2$, respectively (see Appendix 1—table 1). $Pe^{30} < 1$ suggests that nutrient uptake is diffusion-driven in $H = 30 \text{ } \mu\text{m}$. On the contrary, $Pe^{10} \gtrsim 1$ indicates that flow-field-mediated advection may not be overwhelmingly dominant, but nevertheless is significant in enhancing nutrient uptake along with diffusion mediated transport [46].

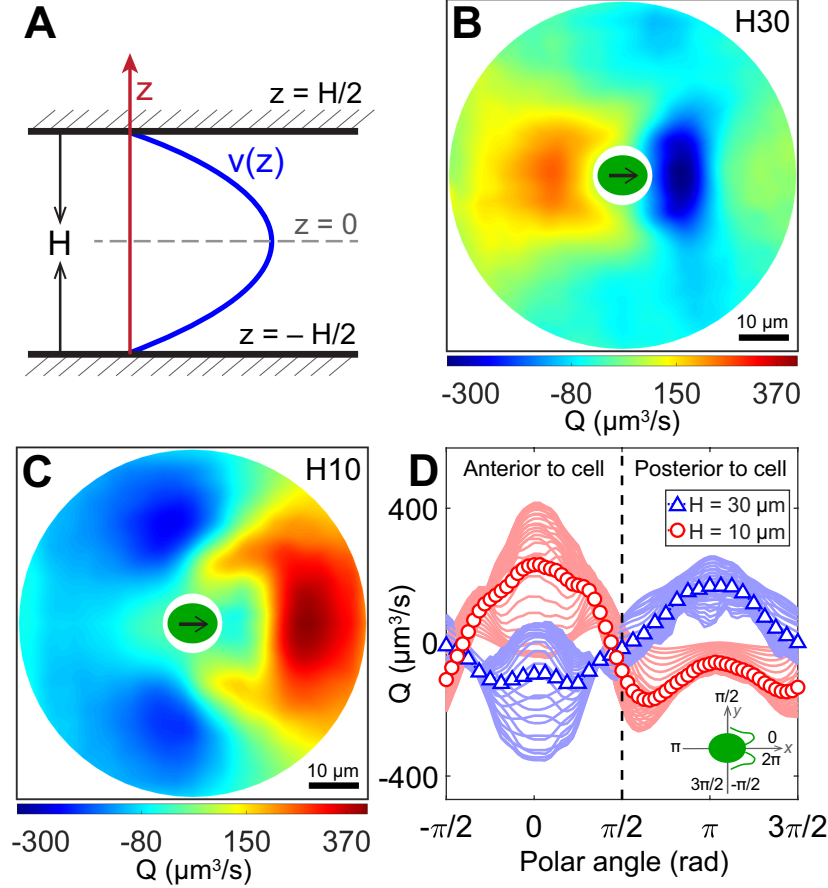


Figure 4. Fluid flux towards confined CR. (A) Schematic of flow profile along z -direction, $v(z) \sim \cos(\pi z/H)$, in a chamber of height H bounded by two solid walls. Volume flux of fluid (z -averaged over cell diameter) towards the cell at each grid point in the $x - y$ plane for the radial distances $r \in [6, 35] \mu\text{m}$ from the cell centre $(0, 0)$ in (B) weak confinement ($H = 30 \mu\text{m}$) and (C) strong confinement ($H = 10 \mu\text{m}$). Black arrows on the cell body indicate that the cells are swimming to the right. The colorbars represent magnitude of volume flux, Q (sign convention: +ve towards the cell & -ve away from the cell). (D) Fluid flux, Q as a function of the polar angle. Solid lines represent the inward volume flux at each radius for the weakly (blue) and strongly (red) confined cell. The correspondingly colored symbols represent the average inward volume flux $Q_{\text{avg}}(\phi) = \langle Q(r, \phi) \rangle_r$ over $r \in [6, 35] \mu\text{m}$. Bottom right inset shows the schematic for polar orientation of the cell.

We now calculate the quantitative enhancement in the volumetric flow rate for the strongly confined cell, which in turn determines the increment in its feeding by absorption and sensing through cell surface and flagella [50, 52]. We consider an effective description of a CR swimming in the $z = 0$ plane of the coordinate system with the first Fourier mode for

the velocity profile along z satisfying the no-slip boundary condition on the solid walls, $\mathbf{v}(x, y, z = \pm H/2) = 0$ (Figure 4A). Therefore, the flow velocity varies as $\mathbf{v}(x, y, z) = \mathbf{v}^0(x, y) \cos(\pi z/H)$ (Figure 4A), where $\mathbf{v}^0 = (v_x, v_y)$ is the flow profile in the swimmer's $x - y$ plane that is experimentally measured in Figure 3.

The volume flow rate, Q , towards the cell is given by the flux of fluid through a cylindrical surface whose axis is along the z -direction. At each polar grid point (r, ϕ) in the $z = 0$ plane of the flow field with the cell centre at origin, we consider the inward radial flow passing through a cylindrical surface of infinitesimal basal perimeter $rd\phi$ and z -averaged over the cell diameter, D . Therefore, the volume flux of fluid or flow rate towards the cell at each grid point is given by

$$Q(r, \phi) = \int_{z=-D/2}^{z=D/2} v_{\text{rad}}(r, \phi, z) r d\phi dz = \bar{v}_{\text{rad}}(r, \phi) D r d\phi \quad (1)$$

where v_{rad} is the radial flow towards the cell and its z -averaged magnitude over the cell diameter is $\bar{v}_{\text{rad}}(r, \phi) = \frac{2v_{\text{rad}}^0(r, \phi)}{\pi D/H} \sin \frac{\pi D}{2H}$. Here, $v_{\text{rad}}^0 = -v_x \cos \phi - v_y \sin \phi$ is the experimentally measured radial flow speed towards the cell at each grid point in the $z = 0$ plane. Using this data from Figure 3, we plot the volume flux of fluid to the weakly (H30) and strongly (H10) confined cell and compare them in Figure 4(B to D).

The colorplots show that the weakly confined CR (H30) moves away from the incoming flow since $Q > 0$ posterior to the cell (Figure 4B,D), whereas the strongly confined cell (H10) swims towards the incoming flow at the cell front (Figure 4C,D). Furthermore, the incoming fluid flux towards the strongly confined CR is significantly enhanced, by about 38%, on comparing the maximum of radially averaged volume flux, $Q_{\text{avg}}(\phi) = \langle Q(r, \phi) \rangle_r$ with that of the weakly confined one in Figure 4D. Together, these plots re-emphasize that the flagella generated feeding currents in the flow are insignificant for the fast swimming cells in weak confinement. In contrast, the opposite vortical flows driven by flagellar beating in strong confinement help in advection dominated fluid transport towards the slowly swimming cell, thereby aiding in its sensing and nutrient uptake, along with the diffusion at smaller spatial scales close to the cell surface.

Theoretical model of strongly confined flow

We begin by using the well-established far-field solution of a parallel Stokeslet between two plates by Liron & Mochon in an attempt to explain the strongly confined CR's flow

field [40]. However, the theoretical flow of Liron & Mochon decays much more rapidly than the experimental one and does not capture the vortex positions and flow variation of the experiment (Appendix 1.4 and Appendix 1—figure 1).

We therefore start afresh from the incompressible 3D Stokes equation, $-\nabla p(\mathbf{r}) + \eta \nabla^2 \mathbf{v}(\mathbf{r}) = 0$, $\nabla \cdot \mathbf{v}(\mathbf{r}) = 0$, where p and \mathbf{v} are the fluid pressure and velocity fields, respectively. Next, we formulate an effective 2D Stokes equation and find its point force solution. Substituting $\mathbf{v}(\mathbf{r}) = \mathbf{v}^0(x, y) \cos(\pi z/H)$, as allowed by the hard-wall boundary conditions (Figure 4A), in the Stokes equation we obtain its quasi-2D Brinkman approximation [39] which, for a point force of strength \mathbf{F} at the $z = 0$ plane, is

$$-\nabla_{xy} p(\mathbf{r}) + \eta \left(\nabla_{xy}^2 - \frac{\pi^2}{H^2} \right) \mathbf{v}(\mathbf{r}) + \mathbf{F} \delta(\mathbf{r}) = 0, \quad \nabla_{xy} \cdot \mathbf{v}(\mathbf{r}) = 0 \quad (2)$$

where p and $\mathbf{v} \equiv \mathbf{v}_0$ are the pressure and fluid velocity in the $x - y$ plane and $\nabla_{xy} = \partial_x \hat{\mathbf{x}} + \partial_y \hat{\mathbf{y}}$. We Fourier transform the above equation in 2D and invoke the orthogonal projection operator $\mathbf{O}_{\mathbf{k}} = 1 - \hat{\mathbf{k}}\hat{\mathbf{k}}$ to annihilate the pressure term and obtain the quasi-2D Brinkman equation in Fourier space

$$\mathbf{v}_{\mathbf{k}} = \frac{\mathbf{O}_{\mathbf{k}} \cdot \mathbf{F}}{\eta \left(k^2 + \frac{\pi^2}{H^2} \right)} \quad (3)$$

We perform inverse Fourier transform on Eq. (3) in 2D for a Stokeslet oriented along the x -direction, $\mathbf{F} = F \hat{\mathbf{x}}$ to obtain its flow field $\mathbf{v}(\mathbf{r})$ at the $z = 0$ plane (Appendix 1.5). We have already shown that superposing this solution for the conventional three point forces at cell centre and flagellar positions of CR which leads to the effective 3-Stokeslet model in 2D is an inappropriate description of the strongly confined flow (Figure 3—figure supplement 1A). This is not surprising at this point because we have quantitatively calculated the force imbalance between the flagellar thrust and cell drag to be $|\mathbf{F}_{th}^{10}|/|\mathbf{F}_{cd}^{10}| \approx 30$, which confirms that the cell is nearly stationary compared to the motion of its flagella. We utilize this experimental insight by superposing only two Stokeslets of strength $-1/2 \hat{\mathbf{x}}$ each at approximate flagellar positions $(x_f, \pm y_f) = (6, \pm 11) \mu\text{m}$ to find qualitatively similar streamlines and vortex flows (Figure 5A) as that of the experimental flow field (Figure 3C). However, this theoretical ‘2-Stokeslet Brinkman flow’ (Figure 5A) decays faster than the experiment as shown in the quantitative comparison of these two flows in Figure 5B. The root mean square deviation (RMSD) between these two flows in v_x , v_y and $|\mathbf{v}|$ are 20.3%, 14.2% and 22.6%, respectively (see Materials and Methods for RMSD definition).

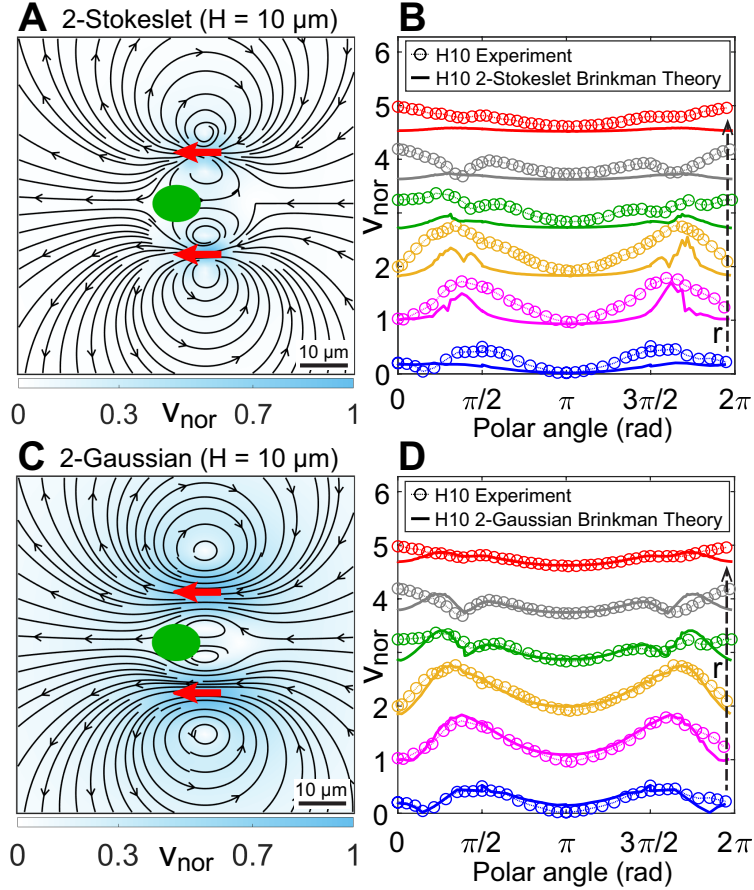


Figure 5. Theoretical flow fields in strong confinement. Theoretically computed flow fields for (A) 2 Stokeslets and (C) 2-Gaussian forces, both positioned at $(6, \pm 11)$ μm (red arrows) using the quasi-2D Brinkman equation for $H = 10$ μm at the $z = 0$ plane. The colorbars represent flow magnitudes normalised by their maximum, v_{nor} . (B) and (D) Comparison of normalised experimental flow of the CR in $H = 10$ μm (Figure 3C) with theoretical flow fields (A) and (C), respectively along representative radial distances, r from the cell centre as a function of polar angle. The convention used for polar angle is same as in Figure 4D. Plots for each r denote the flow magnitudes for those grid points which lie in the radial gap $(r, r + 1)$ μm . From bottom to top, $r = 6, 10, 14, 18, 22, 26$ μm . They are shifted along the y -axis for clarity.

Figure supplement 1. Theoretical flow field due to 3-Gaussian forces in weak confinement.

Figure supplement 2. Correlation in fluid flow.

With the experimental streamlines and vortices well described by a 2-Stokeslet Brinkman model, we now explain the slower flow variation in experiment. Strongly confined experimentally observed flow is mostly ascribed to the flagellar thrust, as described above. Clearly, a delta-function point force will not be adequate to describe the thrust generated by flagellar

beating as they are slender rods of length $L \sim 11 \mu\text{m}$ with high aspect ratio. We, therefore, associate a 2D Gaussian source $g(\mathbf{r}) = \frac{e^{-r^2/2\sigma^2}}{2\pi\sigma^2}$ of standard deviation σ , to Eq. (2) instead of the point-source $\delta(\mathbf{r})$. Thus, the quasi-2D Brinkman equation in Fourier space (3) for a Gaussian force $\mathbf{F}g(\mathbf{r})$ becomes,

$$\mathbf{v}_{\mathbf{k}} = \frac{\mathbf{O}_{\mathbf{k}} \cdot \mathbf{F}}{\eta \left(k^2 + \frac{\pi^2}{H^2} \right)} e^{-k^2\sigma^2/2} . \quad (4)$$

Superposing the inverse Fourier transform of the above equation for two sources of $\mathbf{F} = (-1/2, -1/2) \hat{\mathbf{x}}$ at $(x_f, \pm y_f) = (6, \pm 11) \mu\text{m}$ with $\sigma \sim L/2 = 5 \mu\text{m}$, we obtain the theoretical flow shown in Figure 5C. RMSD in v_x , v_y and $|\mathbf{v}|$ of this theoretical flow with those of the experimental one (Figure 3C) are 7.8%, 9% and 8.3%, respectively. Comparing these two flows along representative radial distances from the cell centre as a function of polar angle show a good agreement (Figure 5D). Notably, Figure 5C, i.e., the ‘2-Gaussian Brinkman flow’, has captured the flow variation and most of the experimental flow features accurately. Specifically, these are the lateral vortices at $20 \mu\text{m}$ and an anterior stagnation point at $13 \mu\text{m}$ from cell centre. The only limitation of this theoretical model is that it cannot account for the front-back asymmetry of the strongly confined flow, as is evident from Figure 5C for the polar angles 0 or 2π and π which correspond to front and back of the cell, respectively. This deviation is more pronounced in the frontal region as the cell body squashed between the two solid walls mostly blocks the forward flow from reaching the cell posterior. Thus, the no-slip boundary on the cell body needs to be invoked to mimic the front-back flow asymmetry, which is a more involved analysis due to the presence of multiple boundaries and can be addressed in a follow-up study.

Now that we have explained the flow field of CR in strong confinement, we test our quasi-2D Brinkman theory in weak confinement, $H = 30 \mu\text{m}$, where the thrust and drag forces almost balance each other. Hence, we use the conventional 3-Stokeslet model for CR, but with a Gaussian distribution for each point force. We, therefore, superpose the solution of Eq. (4) for 3-Gaussian forces representing the cell body and two flagella in $H = 30 \mu\text{m}$. The resulting flow field (Figure 5—figure supplement 1) matches qualitatively with the experimental flow field of CR in weak confinement (Figure 3A). This deviation is expected in weak confinement, $D/H \sim 0.3$, because the quasi-2D theoretical approximation is mostly valid at $D/H \gtrsim 1$, even though RMSD in v_x , v_y and $|\mathbf{v}|$ remains in the low range at 11.4%, 11.2% and 13.8%, respectively.

We now calculate the normalised spatial velocity-velocity correlation function of these flows, $C_{vv}(R) = \frac{\langle \mathbf{v}(r) \cdot \mathbf{v}(r + R) \rangle}{\langle \mathbf{v}(r) \cdot \mathbf{v}(r) \rangle}$ to estimate the enhancement in fluid mixing in strong confinement which is also evident in the videos of cell suspensions containing tracer particles (Video 1 and Figure 5—figure supplement 2). The characteristic decay length scale of flows, λ , is 13.2 μm for the strongly confined flow, which is 37.5% higher than the weakly confined flow in $H = 30 \mu\text{m}$ ($\lambda = 9.6 \mu\text{m}$), even though the cell is swimming very slowly in strong confinement.

DISCUSSION

Our results show that a prototypical active microalga like CR under strong confinement has a motility and flow field strikingly different from that of a bulk swimmer, leading to enhanced fluid mixing. The decrease in cell speed with increasing confinement, which arises due to mechanical friction from the walls and not due to behavioural change, leads to lateral flow vorticity opposite to that observed in bulk or weak confinement. This is the first example of a strongly confined microswimmer whose far-field flow is that of a 2D source dipole pointing *opposite* to the cell’s swimming direction. This result is contrary to the common theoretical expectation that the far-field flow of a confined microswimmer between two closely spaced solid walls is a 2D source dipole pointing *along* the swimmer’s propulsion direction [15, 19]. These experimental results establish that confinement not only alters the hydrodynamics but also modifies the swimmer motility which in turn impacts the fluid flows. This coupling between confinement and motility is typically ignored in theoretical studies because the focus tends to be on the effect of confining geometry on flow-fields induced by a given set of force-generators [15, 19], which is appropriate for weak confinement, whereas strong confinement alters the complexion of forces generating the flow. Recent experimental reports have not observed the effect we discuss because they confine CR in tall and soft PDMS chambers ($D/H \lesssim 0.7$), which amounts to weak confinement [12]. Theoretically, a 2-Gaussian Brinkman model describes strongly confined CR flows far more effectively than the conventional 3-Stokeslet model. Our theoretical approach can also be easily utilised to analyse flows of a dilute collection of strongly confined swimmers (Appendix 1.6 and Appendix 1—figure 2).

We note that even though CR is known to glide on liquid-infused solid substrates through flagella-mediated adhesive interactions [27], it has recently been shown that the strength

of flagellar adhesion is sensitive to and switchable by ambient light [49]. Consequently, it is likely that CR in its natural habitat of rocks and soils would also utilise swimming in addition to gliding. Our quantitative analysis shows that despite the higher frictional drag due to the strongly confining walls, there is 38% increment in fluid flux towards the H10 cell. That is, the inverse vortical flows driven by the flagellar propulsive thrust enhance the mass transport of nutrients to the strongly confined microswimmer. This suggests that swimming is more efficient than gliding for CR under strong confinement (specially in low-light conditions), even though CR speeds are of the same order in both these mechanisms ($u_{glide} \sim 1 \mu\text{m/s}$ [27] and $u_{swim} \sim 4 \mu\text{m/s}$).

Finally, our experimental and theoretical methodologies are completely general and can be applied to any strongly confined microswimmer, biological or synthetic from individual to collective scales. Specifically, our robust and efficient description using point/Gaussian forces in a quasi-2D Brinkman equation is simple enough to implement and analyse confined flows in a wide range of active systems. We expect our work to inspire further studies on biomechanics and fluid mixing due to hard wall confinement of concentrated active suspensions [14, 25]. These effects can be exploited in realizing autonomous motion through microchannel for biomedical applications and in microfluidic devices for efficient control, navigation and trapping of microbes and synthetic swimmers [18, 53, 54].

MATERIALS AND METHODS

Surface modification of microspheres and glass surfaces

CR cells are synchronously grown in 12:12 hour light:dark cycle in Tris-Acetate-Phosphate (TAP+P) medium. This culture medium contains divalent ions such as Ca^{2+} , Mg^{2+} , SO_4^{2-} which decrease the screening length of the 200 nm negatively charged microspheres, thereby promoting inter-particle aggregation and sticking to glass surfaces and CR's flagella. Therefore, the sulfate latex microspheres (S37491, Thermo Scientific) are sterically stabilised by grafting long polymer chains of polyethylene glycol (mPEG-SVA-20k, NANOCS, USA) with the help of a positively charged poly-L-lysine backbone (P7890, 15-30kDa, Sigma) [30]. In addition, the coverslip and slide surfaces are also cleaned and coated with polyacrylamide brush to prevent non-specific adhesion of microspheres and flagella to the glass surfaces,

prior to sample injection [30].

Sample imaging

Cell suspension is collected in the logarithmic growth phase within the first 2-3 hours of light cycle and re-suspended in fresh TAP+P medium. After 30 minutes of equilibration, the cells are injected into the sample chamber. The sample chamber containing cells and tracers is mounted on an inverted microscope (Olympus IX83/IX73) and placed under red light illumination (> 610 nm) to prevent adhesion of flagella [49] and phototactic response of CR [55]. We let the system acclimatize in this condition for 40 minutes before recording any data. All flow field data, flagellar waveform and cellular trajectory (except for Figure 2A) are captured using a 40X phase objective (Olympus, 0.65 NA, Plan N, Ph2) coupled to a high speed CMOS camera (Phantom Miro C110, Vision Research, pixel size = $5.6 \mu\text{m}$) at 500 frames/s. As CR cells move faster in $H = 30 \mu\text{m}$ chamber, a 8.2 second long trajectory cannot be captured at that magnification. So we used a 10X objective in bright field (Olympus, 0.25 NA, PlanC N) connected to a high speed camera of higher pixel length (pco.1200hs, pixel size = $12 \mu\text{m}$) at 100 frames/s to capture 8.2 s long trajectories of H30 cells (Figure 2A).

Our observations are consistent across CR cultures grown on different days and cultures inoculated from different colonies of CR agar plates. We have prepared at least 15-18 samples of dilute CR suspensions from 8 different days/batches of cultures, each for chambers of height 10 and $30 \mu\text{m}$. Our imaging parameters remain same for all observations. We also use the same code, which is verified from standard particle tracking videos, for tracking all the cells. We modify the cell tracking code to track the tracer motion for calculating the flow-field data.

Height measurement of sample chamber

We use commercially available double tapes of thickness 10 and $30 \mu\text{m}$ (Nitto Denko Corporation) as spacer between the glass slide and coverslip. To measure the actual separation between these two surfaces, we stick 200 nm microspheres to a small strip ($18 \times 6 \text{ mm}^2$) on both the glass surfaces by heating a dilute solution of microspheres. Next, we inject immersion oil inside the sample chamber to prevent geometric distortion due to refractive index

mismatch between objective immersion medium and sample. The chamber height is then measured by focusing the stuck microspheres on both surfaces through a 60X oil-immersion phase objective (Olympus, 1.25 NA). We find the measured chamber height for the 10 μm spacer to be $10.88 \pm 0.68 \mu\text{m}$ and for the 30 μm spacer to be $30.32 \pm 0.87 \mu\text{m}$, from 8 different samples in each case.

Particle Tracking Velocimetry (PTV)

The edge of a CR cell body appears as a dark line (Figure 1C to E) in phase contrast microscopy and is detected using ridge detection in ImageJ [56]. An ellipse is fitted to the pixelated CR's edge and the major axis vertex in between the two flagellum is identified through custom-written MATLAB codes. The cell body is masked and the tracers' displacement in between two frames (time gap, 2 ms) are calculated in the lab frame using standard MATLAB tracking routines [57]. The velocity vectors obtained from multiple beat cycles are translated and rotated to a common coordinate system where the cell's major axis vertex is pointing to the right (Figure 3A,C). Outliers with velocity magnitude more than six standard deviations from the mean are deleted. The resulting velocity vectors from all beat cycles (including those from different cells in $H = 30 \mu\text{m}$) are then placed on a mesh grid of size $2.24 \times 2.24 \mu\text{m}^2$ and the mean at each grid point is computed. The gridded velocity vectors are then smoothed using a 5×5 averaging filter. Furthermore, for comparison with theoretical flow, the x and y components of the velocity vectors are interpolated on a gridsize of $1 \times 1 \mu\text{m}^2$. Streamlines are plotted using the '*streamslice*' function in MATLAB.

Trajectory tortuosity

Tortuosity characterizes the number of twists or loops in a cell's trajectory. It is given by the ratio of arclength to end-to-end distance between two points in a trajectory. We divide each trajectory into segments of arc-length $\approx 20 \mu\text{m}$. We calculate the tortuosity for individual segments and find their mean for each trajectory. We consider the trajectories of all cells whose mean speed $> 1 \mu\text{m/s}$ and are imaged at 500 frames/s through 40X objective for consistency. There were 52 H30 cells, 35 H10 Wobblers and 23 H10 Synchronous cells which satisfied these conditions and the data from these cells constitute Figure 2G.

Root Mean Square Deviation (RMSD)

The match between experimental and theoretical flow fields is quantified by the root-mean-square deviation (RMSD) of their velocities in the normalised scale (v/v_{\max}). $RMSD = \sqrt{\sum_{j=1}^{NG} (v_j^{\text{expt}} - v_j^{\text{th}})^2 / NG}$, where v_j^{expt} and v_j^{th} are the experimental and theoretical values of the velocity fields at the j -th grid point, respectively and NG is the total number of grid points. We calculate RMSD in the x and y components of the flow velocity i.e. in v_x and v_y , respectively for a comparison of the vector nature of the flow fields. This is because, the signed magnitudes of v_x and v_y determine the vector direction of the flow. We also calculate RMSD in the flow speed ($|\mathbf{v}| = [v_x^2 + v_y^2]^{1/2}$) to compare their scalar magnitudes.

Acknowledgements: We acknowledge Aparna Baskaran, Ramin Golestanian, Ayantika Khanra, Malay Pal, Balachandra Suri and Ronojoy Adhikari for useful discussions.

Funding: This work is supported by the DBT/Wellcome Trust India Alliance Fellowship [grant number IA/I/16/1/502356] awarded to P.S. S.R. acknowledges support from a J C Bose Fellowship of the SERB (India) and from the Tata Education and Development Trust.

Author Contributions: D.M. and P.S. conceived and designed the experiments. S.R. proposed the theoretical model. D.M. performed experiments, data analysis and theoretical computations. A.G.P. carried out theoretical calculations at the initial stages of this work. D.M., P.S. and S.R. interpreted the experiments and wrote the manuscript.

Competing financial interests: The authors declare no competing financial interests.

-
- [1] E. Lauga and T. R. Powers. The hydrodynamics of swimming microorganisms. *Reports on Progress in Physics*, 72(9):096601, aug 2009.
 - [2] T. J. Pedley and J. O. Kessler. Hydrodynamic phenomena in suspensions of swimming microorganisms. *Annual Review of Fluid Mechanics*, 24(1):313–358, 1992.
 - [3] J. Elgeti, R. G. Winkler, and G. Gompper. Physics of microswimmers-single particle motion and collective behavior: a review. *Reports on Progress in Physics*, 78(5):056601, apr 2015.
 - [4] C. Bechinger, R. Leonardo, H. Lowen, C. Reichhardt, and G. Volpe. Active particles in complex and crowded environments. *Reviews of Modern Physics*, 88:045006, 2016.

- [5] P. Denissenko, V. Kantsler, D. J. Smith, and J. Kirkman-Brown. Human spermatozoa migration in microchannels reveals boundary-following navigation. *Proceedings of the National Academy of Sciences*, 109(21):8007–8010, 2012.
- [6] T. Bhattacharjee and S. S. Datta. Bacterial hopping and trapping in porous media. *Nature Communications*, 10(1):2075, May 2019.
- [7] B. Qin, C. Fei, A. A. Bridges, A. A. Mashruwala, H. A. Stone, N. S. Wingreen, and B. L. Bassler. Cell position fates and collective fountain flow in bacterial biofilms revealed by light-sheet microscopy. *Science*, 369(6499):71–77, 2020.
- [8] D. Hoh, S. Watson, and E. Kan. Algal biofilm reactors for integrated wastewater treatment and biofuel production: A review. *Chemical Engineering Journal*, 287:466 – 473, 2016.
- [9] W. Foissner. An updated compilation of world soil ciliates (protozoa, ciliophora), with ecological notes, new records, and descriptions of new species. *European Journal of Protistology*, 34(2):195–235, 1998.
- [10] N. Heddergott, T. Krüger, S. B. Babu, A. Wei, E. Stellamanns, S. Uppaluri, T. Pfohl, H. Stark, and M. Engstler. Trypanosome motion represents an adaptation to the crowded environment of the vertebrate bloodstream. *PLOS Pathogens*, 8(11):1–17, 11 2012.
- [11] W. M. Durham, J. O. Kessler, and R. Stocker. Disruption of vertical motility by shear triggers formation of thin phytoplankton layers. *Science*, 323(5917):1067–1070, 2009.
- [12] R. Jeanneret, D. O. Pushkin, and M. Polin. Confinement enhances the diversity of microbial flow fields. *Phys. Rev. Lett.*, 123:248102, Dec 2019.
- [13] T. Ostapenko, F. J. Schwarzendahl, T. J. Bøddeker, C. T. Kreis, J. Cammann, M. G. Mazza, and O. Bäümchen. Curvature-guided motility of microalgae in geometric confinement. *Phys. Rev. Lett.*, 120:068002, Feb 2018.
- [14] H. Kurtuldu, J. S. Guasto, K. A. Johnson, and J. P. Gollub. Enhancement of biomixing by swimming algal cells in two-dimensional films. *Proceedings of the National Academy of Sciences*, 108(26):10391–10395, 2011.
- [15] T. Brotto, J.-B. Caussin, E. Lauga, and D. Bartolo. Hydrodynamics of confined active fluids. *Phys. Rev. Lett.*, 110:038101, Jan 2013.
- [16] A. Maitra, P. Srivastava, M. C. Marchetti, S. Ramaswamy, and M. Lenz. Swimmer suspensions on substrates: Anomalous stability and long-range order. *Phys. Rev. Lett.*, 124:028002, Jan 2020.
- [17] W. Duan, W. Wang, S. Das, V. Yadav, T. E. Mallouk, and A. Sen. Synthetic nano- and

- micromachines in analytical chemistry: Sensing, migration, capture, delivery, and separation. *Annual Review of Analytical Chemistry*, 8(1):311–333, 2015.
- [18] F. Z. Temel and S. Yesilyurt. Confined swimming of bio-inspired microrobots in rectangular channels. *Bioinspiration & biomimetics*, 10(1):016015, 2015.
- [19] A. J. T. M. Mathijssen, A. Doostmohammadi, J. M. Yeomans, and T. N. Shendruk. Hydrodynamics of micro-swimmers in films. *Journal of Fluid Mechanics*, 806:35–70, 2016.
- [20] I. H. Riedel, K. Kruse, and J. Howard. A self-organized vortex array of hydrodynamically entrained sperm cells. *Science*, 309(5732):300–303, 2005.
- [21] A. P. Petroff, X.-L. Wu, and A. Libchaber. Fast-moving bacteria self-organize into active two-dimensional crystals of rotating cells. *Phys. Rev. Lett.*, 114:158102, Apr 2015.
- [22] A. C. H. Tsang and E. Kanso. Density shock waves in confined microswimmers. *Phys. Rev. Lett.*, 116:048101, Jan 2016.
- [23] Rothschild. Non-random distribution of bull spermatozoa in a drop of sperm suspension. *Nature*, 198(4886):1221–1222, 1963.
- [24] R. A. Lambert, F. Picano, W.-P. Breugem, and L. Brandt. Active suspensions in thin films: nutrient uptake and swimmer motion. *Journal of Fluid Mechanics*, 733:528–557, 2013.
- [25] D. O. Pushkin and J. M. Yeomans. Stirring by swimmers in confined microenvironments. *Journal of Statistical Mechanics: Theory and Experiment*, 2014(4):P04030, apr 2014.
- [26] A. Persat, C. D. Nadell, M. K. Kim, F. Ingremeau, A. Siryaporn, K. Drescher, N. S. Wingreen, B. L. Bassler, Z. Gitai, and H. A. Stone. The mechanical world of bacteria. *Cell*, 161(5):988–997, May 2015.
- [27] S. Sasso, H. Stibor, M. Mittag, and A. R. Grossman. The natural history of model organisms: From molecular manipulation of domesticated *Chlamydomonas reinhardtii* to survival in nature. *eLife*, 7:e39233, nov 2018.
- [28] D. R. Brumley, R. Rusconi, K. Son, and R. Stocker. Flagella, flexibility and flow: Physical processes in microbial ecology. *The European Physical Journal Special Topics*, 224(17):3119–3140, Dec 2015.
- [29] S. K. Choudhary, A. Baskaran, and P. Sharma. Reentrant efficiency of phototaxis in *chlamydomonas reinhardtii* cells. *Biophysical Journal*, 117(8):1508 – 1513, 2019.
- [30] D. Mondal, R. Adhikari, and P. Sharma. Internal friction controls active ciliary oscillations near the instability threshold. *Science Advances*, 6(33), 2020.
- [31] R. E. Goldstein. Green algae as model organisms for biological fluid dynamics. *Annual Review*

- of *Fluid Mechanics*, 47(1):343–375, 2015.
- [32] C. Brennen and H. Winet. Fluid mechanics of propulsion by cilia and flagella. *Annual Review of Fluid Mechanics*, 9(1):339–398, 1977.
- [33] S. Rafai, L. Jibuti, and P. Peyla. Effective viscosity of microswimmer suspensions. *Phys. Rev. Lett.*, 104:098102, Mar 2010.
- [34] M. I. Khan, J. H. Shin, and J. D. Kim. The promising future of microalgae: current status, challenges, and optimization of a sustainable and renewable industry for biofuels, feed, and other products. *Microbial cell factories*, 17(1):36–36, Mar 2018.
- [35] S. K. Min, G. H. Yoon, J. H. Joo, S. J. Sim, and H. S. Shin. Mechanosensitive physiology of *Chlamydomonas reinhardtii* under direct membrane distortion. *Scientific Reports*, 4(1):4675, Apr 2014.
- [36] S.-M. Paik. *Biomass Enhancement in Chlamydomonas reinhardtii using Steady C/N Ratio Microfluidic Perfusion Bioreactor, Vibrational Stress Priming, and Malate Synthase Expression*. PhD thesis, Aug 2018.
- [37] J. S. Guasto, K. A. Johnson, and J. P. Gollub. Oscillatory flows induced by microorganisms swimming in two dimensions. *Phys. Rev. Lett.*, 105:168102, Oct 2010.
- [38] K. Drescher, R. E. Goldstein, N. Michel, M. Polin, and I. Tuval. Direct measurement of the flow field around swimming microorganisms. *Phys. Rev. Lett.*, 105:168101, Oct 2010.
- [39] H. C. Brinkman. A calculation of the viscous force exerted by a flowing fluid on a dense swarm of particles. *Flow, Turbulence and Combustion*, 1(1):27, 1949.
- [40] N. Liron and S. Mochon. Stokes flow for a stokeslet between two parallel flat plates. *Journal of Engineering Mathematics*, 10(4):287–303, 1976.
- [41] M. Polin, I. Tuval, K. Drescher, J. P. Gollub, and R. E. Goldstein. *Chlamydomonas* swims with two “gears” in a eukaryotic version of run-and-tumble locomotion. *Science*, 325(5939):487–490, 2009.
- [42] A. Qin, B. and Gopinath, J. Yang, J. P. Gollub, and P. E. Arratia. Flagellar kinematics and swimming of algal cells in viscoelastic fluids. *Scientific Reports*, 5(1):9190, 2015.
- [43] L. Jibuti, W. Zimmermann, S. Rafai, and P. Peyla. Effective viscosity of a suspension of flagellar-beating microswimmers: Three-dimensional modeling. *Phys. Rev. E*, 96:052610, Nov 2017.
- [44] B. M. Friedrich and F. Jülicher. Flagellar synchronization independent of hydrodynamic interactions. *Phys. Rev. Lett.*, 109:138102, Sep 2012.

- [45] R. R. Bennett and R. Golestanian. Emergent run-and-tumble behavior in a simple model of chlamydomonas with intrinsic noise. *Phys. Rev. Lett.*, 110:148102, Apr 2013.
- [46] D. Tam and A. E. Hosoi. Optimal feeding and swimming gaits of biflagellated organisms. *Proceedings of the National Academy of Sciences*, 108(3):1001–1006, 2011.
- [47] T. Kiørboe. *A Mechanistic Approach to Plankton Ecology*. Princeton University Press, 2008.
- [48] J. S. Guasto, R. Rusconi, and R. Stocker. Fluid mechanics of planktonic microorganisms. *Annual Review of Fluid Mechanics*, 44(1):373–400, 2012.
- [49] C. T. Kreis, M. Le Blay, C. Linne, M. M. Makowski, and O. Bäümchen. Adhesion of chlamydomonas microalgae to surfaces is switchable by light. *Nature Physics*, 14(1):45–49, 2018.
- [50] Y. Ding, J. C. Nawroth, M. J. McFall-Ngai, and E. Kanso. Mixing and transport by ciliary carpets: a numerical study. *Journal of Fluid Mechanics*, 743:124–140, 2014.
- [51] O. H. Shapiro, V. I. Fernandez, M. Garren, J. S. Guasto, F. P. Debaillon-Vesque, E. Kramarsky-Winter, A. Vardi, and R. Stocker. Vortical ciliary flows actively enhance mass transport in reef corals. *Proceedings of the National Academy of Sciences*, 111(37):13391–13396, 2014.
- [52] N. Osterman and A. Vilfan. Finding the ciliary beating pattern with optimal efficiency. *Proceedings of the National Academy of Sciences*, 108(38):15727–15732, 2011.
- [53] B.-W. Park, J. Zhuang, O. Yasa, and M. Sitti. Multifunctional bacteria-driven microswimmers for targeted active drug delivery. *ACS Nano*, 11(9):8910–8923, Sep 2017.
- [54] A. Karimi, S. Yazdi, and A. M. Ardekani. Hydrodynamic mechanisms of cell and particle trapping in microfluidics. *Biomicrofluidics*, 7(2):21501–21501, 2013.
- [55] O. A. Sineshchekov, K.-H. Jung, and J. L. Spudich. Two rhodopsins mediate phototaxis to low- and high-intensity light in chlamydomonas reinhardtii. *Proceedings of the National Academy of Sciences*, 99(13):8689–8694, 2002.
- [56] T. Wagner and M. Hiner. thorstenwagner/ij-ridgedetection: Ridge detection 1.4.0. *Detect ridges/lines with ImageJ: Ridge Detection 1.4.0*, Aug 2017.
- [57] D. Blair and E. Dufresne. The matlab particle tracking code repository. *Particle-tracking code available at <http://physics.georgetown.edu/matlab>*, 2008.
- [58] S. Bhattacharya, J. Bławdziewicz, and E. Wajnryb. Hydrodynamic interactions of spherical particles in suspensions confined between two planar walls. *Journal of Fluid Mechanics*, 541:263–292, 2005.
- [59] I. S. Gradshteyn and I. M. Ryzhik. *Table of integrals, series, and products*. Elsevier/Academic

Press, Amsterdam, 7th edition, 2007.

FIGURE SUPPLEMENTS

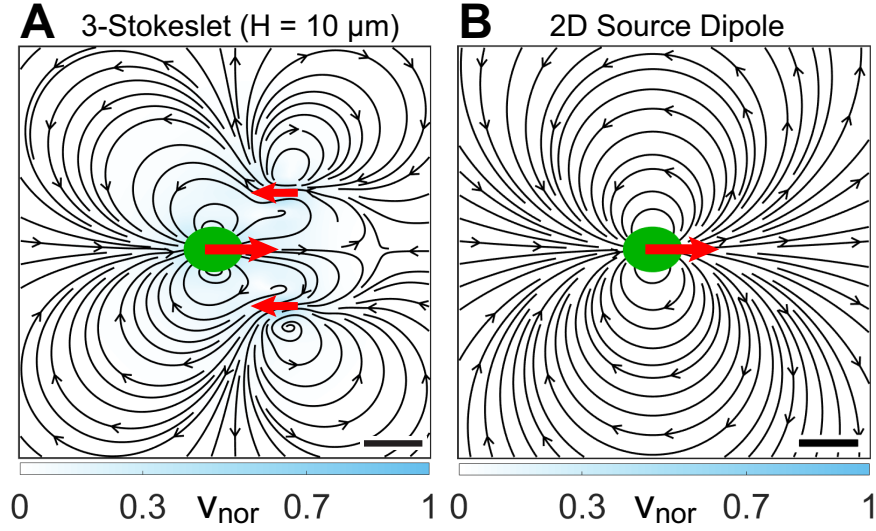


Figure 3—figure supplement 1. Expected flow fields of a strongly confined CR using conventional theoretical approaches. (A) Theoretically computed *near-field flow* characteristics as expected from the screened version of the bulk flow field i.e. from the 3-Stokeslet model in $H = 10 \mu\text{m}$. The 3 Stokeslets denoted by red arrows represent the cell drag of strength $+1$ at $(0,0)$ and flagellar thrust of strength $-1/2$ each at $(12, \pm 10) \mu\text{m}$. This flow field is calculated using the quasi-2D Brinkman equation, which is introduced later in this article. (B) Theoretically predicted *far-field flow* of a microswimmer in confinement which is that of a 2D source dipole oriented along the propulsion direction (denoted by red arrow) [15, 19]. The colorbars represent flow magnitudes normalised by their maximum, v_{nor} . Scalebar, $10 \mu\text{m}$.

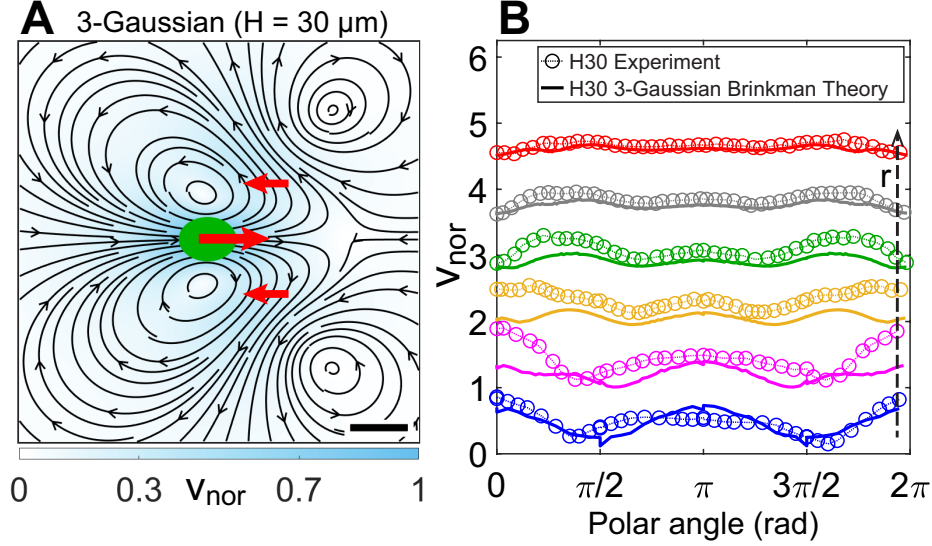


Figure 5—figure supplement 1. Theoretical flow field due to 3-Gaussian forces in weak confinement. (A) Theoretically computed flow field from 3-Gaussian forces (cell drag of strength $+1$ at $(0,0)$, flagellar thrust of strength $-1/2$ each at $(12, \pm 10)$ μm ; all denoted by red arrows) using the quasi-2D Brinkman equation for $H = 30$ μm at the $z = 0$ plane. The Gaussian standard deviation, σ for cell and flagellum are 3 and 5 μm , respectively. The colorbar represents flow magnitude normalised by its maximum, v_{nor} . Scalebar, 10 μm . (B) Comparison between normalised experimental (Figure 3A) and theoretical flow field (A) of a cell swimming in $H = 30$ μm along representative radial distances, r from the cell centre as a function of polar angle. Schematic of the polar orientation of CR is shown in the bottom right inset of Figure 4D. Plots for each r denote the flow magnitudes for those grid points which lie in the radial gap $(r, r + 1)$ μm . From bottom to top, $r = 6, 10, 14, 18, 22, 26$ μm . They are shifted along the y -axis for clarity. RMSD between experimental and theoretical flow magnitudes is 13.8% .

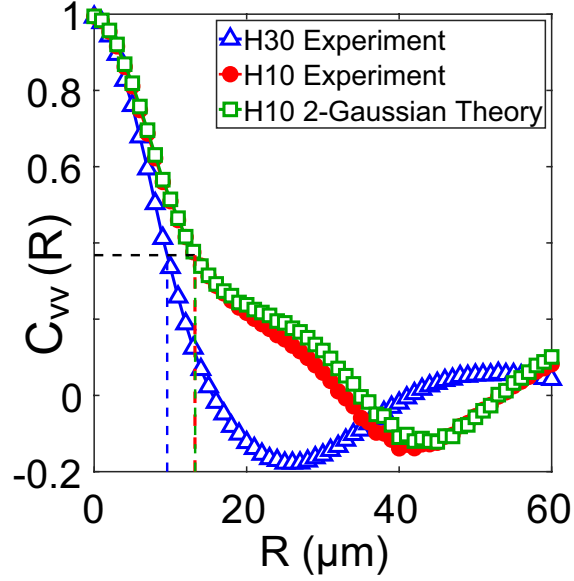


Figure 5—figure supplement 2. Correlation in fluid flow. Normalised radial velocity-velocity correlation function, $C_{vv}(R)$, of flow fields in Figures 3A,C and 5C. The dashed vertical lines denote the characteristic length scales, λ , for flows where the correlation function decays to $1/e$ (horizontal dashed line). $\lambda = 9.6 \mu\text{m}$ for the weakly confined flow (H30) and $\lambda = 13.2 \mu\text{m}$ for the strongly confined flow (H10), both experiment and theory.

VIDEO CAPTIONS

Video 1. Video of a strongly confined *Chlamydomonas* cell swimming with synchronous beat in presence of tracers. High speed video microscopy of a strongly confined swimmer (synchronously beating *Chlamydomonas* cell in $H = 10 \mu\text{m}$ chamber) in presence of tracer particles at 500 frames/s. This phase-contrast video clearly shows the synchronous breaststroke and planar beating of flagella with intermittent phase slips. This is the representative cell whose flow field is shown in Figure 3C. The direction of vortex flow is evident from the tracers' motion.

Video 2. Video of wobbling *Chlamydomonas* cells with asynchronous or paddling flagellar beat. Flagellar waveform of *Chlamydomonas* cells in $H = 10 \mu\text{m}$ chamber with wobbling cell body i.e. H10 Wobblers. The video is divided into 3 parts. The first part shows the asynchronous and planar flagellar beat of a cell which leads to a wobbling motion of the cell body. The second part shows the distinctive paddling flagellar beat of a cell, anterior to the cell body. Here, the flagellar beat plane is perpendicular to the imaging $x - y$ plane and one of the flagella is mostly out of focus. In both these cases, the cell bodies wobble due to their irregular flagellar beat pattern. The third part shows a representative H10 Wobbler which switches from paddling beat to an asynchronous one.

Video 3. Video of a weakly confined *Chlamydomonas* cell swimming in presence of tracers. High speed video microscopy of a weakly confined *Chlamydomonas* cell swimming in $H = 30 \mu\text{m}$ chamber in presence of tracer particles at 500 frames/s. This movie shows the natural motility of cells in bulk where they spin about their body axis. The movie starts with the cell and its flagella beating in the image plane. At $\sim 90 - 180$ ms, the flagellar beat of the cell is out of the image plane, when the cell body is rotating about its axis. The flow field is calculated only when the flagellar beat of the H30 cell is in the image plane, i.e. for $0 - 90$ ms and $180 - 252$ ms for this particular video.

APPENDIX 1

1.1. Power dissipated through the flow fields

In low-Reynolds-number flows, the power P generated by a microswimmer is dissipated through the induced flow fields as $P = 2\eta \int_V (\mathbf{\Gamma} : \mathbf{\Gamma}) dV$ [37]. Here, η is the fluid viscosity, $\mathbf{\Gamma} = \frac{1}{2}[\nabla\mathbf{v} + (\nabla\mathbf{v})^T]$ is the fluid strain rate due to gradients in the flow velocity \mathbf{v} , and the integral is over the quasi-2D chamber of height H . Roughly, for flows in bulk or in soft 2D films, the velocity gradient along the chamber height is negligible and only the 2×2 part of $\mathbf{\Gamma}$ corresponding to directions in the plane perpendicular to the confinement direction has non-negligible components [37]. This is not true in our case because the rigid boundaries act as momentum sinks, imposing a significant gradient in the fluid flow along the confinement direction z . Since the flow velocity varies as $\mathbf{v}(x, y, z) = \mathbf{v}^0(x, y) \cos(\pi z/H)$ (refer to Figure 4A and associated main text), the norm-squared of the strain rate tensor for hard-wall confined flows is given by $\mathbf{\Gamma} : \mathbf{\Gamma} = (\mathbf{\Gamma} : \mathbf{\Gamma})^{\text{bulk}} + \frac{(\pi v^0)^2}{2H^2} \sin^2\left(\frac{\pi z}{H}\right)$ where $(\mathbf{\Gamma} : \mathbf{\Gamma})^{\text{bulk}} = (\partial_x v_x)^2 + \frac{1}{2}(\partial_y v_x + \partial_x v_y)^2 + (\partial_y v_y)^2$ and $\mathbf{v}^0 = (v_x, v_y)$ is the flow profile in the swimmer's $x-y$ plane that is experimentally measured in Figure 3. We calculate the viscous power dissipation from the beat-averaged flow fields of CR to be $P^{30} = 0.78$ fW in weak confinement and $P^{10} = 1.05$ fW in strong confinement. These values are of the same order for both types of confinement and also to that measured for CR in soft fluid films ($P_{\text{mean flow}}$ in Fig. 4a of [37]).

1.2. Can lubrication theory account for the additional frictional drag from the walls in the strongly confined case?

In strong confinement, the cells are steadily swimming at mean speed of $u^{10} \approx 4 \mu\text{m/s}$ where the H10 cell body is in close proximity to the rigid walls. In this limiting case of $D/H \sim 1$, Faxen's iterative series solution is inadequate and hence we use the asymptotic, lubrication-theory solution to the Stokes equation [58] for calculating the effective friction coefficient of a moving sphere in presence of walls. The correction factor to the Stokes drag for a sphere translating (*parallel to the walls*) at mid-way between two parallel walls in the lubrication regime is $\eta_L = -\frac{16}{15} \log\left(\frac{\delta}{D/2}\right) + 1.45$ (Eq. 7.5a of [58]), where $\delta = (H - D)/2$ is the height of the lubrication layer at each cell-wall interface. If the cell-motion-induced

shear flow of the fluid film in this layer is the origin of the wall friction force in the strongly confined case, then the effective drag on the near-spherical cell body due to two cell-wall lubrication regions, $|\mathbf{F}_{drag}^{10}| = 3\pi\eta Du^{10} \eta_L$ would be enough to balance the flagellar thrust force in H10, $|\mathbf{F}_{th}^{10}| \approx 11.31$ pN. On equating these two, we calculate $\eta_L \approx 29.76$ which gives an estimate of $\delta \sim 1.49 \times 10^{-8}$ nm for the height of the lubrication layer. This is too small to contain any water molecule as its diameter is 0.28 nm. Hence, lubrication theory cannot account for the additional frictional drag from the walls suggesting that this drag is not fluidic in nature and the cell body is likely in direct contact with the strongly confining walls.

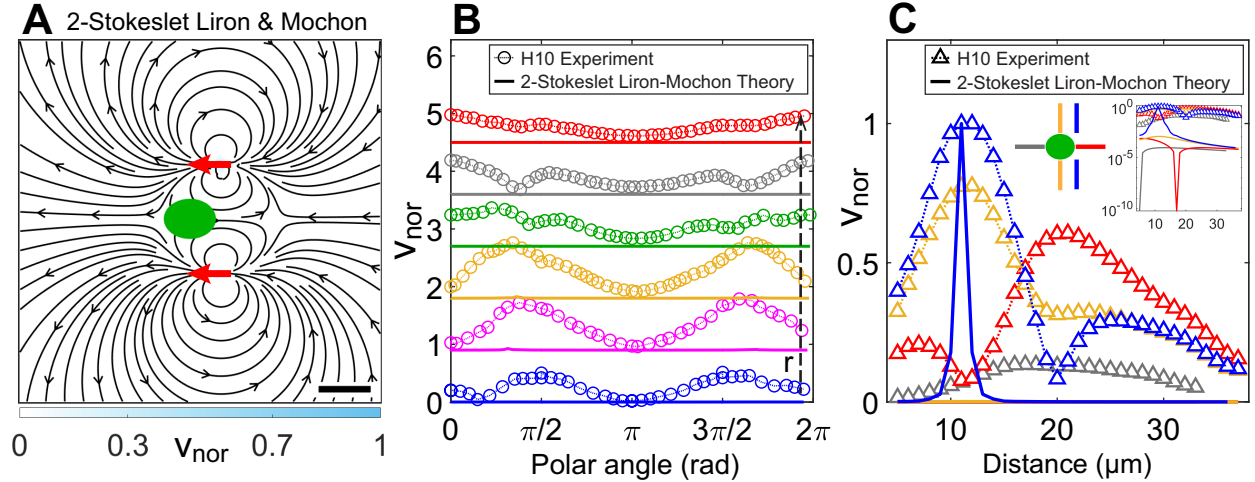
1.3. Swimmer based Péclet number

Generally, speed and length scales in the definition of Péclet number are given by the swimmer speed, u , and radius, R which we refer to as the swimmer based Péclet number, $Pe_c = uR/D_S$. By this definition, $Pe_c^{30} \approx 0.6$ and $Pe_c^{10} = 0.02$ for the weakly and strongly confined CR, respectively. However, we note that the flow field closer to the cell surface is dominated by the vortices lateral to the cell body (Figure 3A,C), whose magnitude is significantly higher than the swimmer speed for the strongly confined cell ($V/u \sim 11$), in contrast to that of the weakly confined cell ($V/u \sim 0.3$). Hence, the flow based Péclet number is more pertinent for the strongly confined cell ($H = 10 \mu\text{m}$), which is shown below (Appendix 1—table 1) to be 100 times higher than the swimmer based Péclet number, whereas both definitions yield almost similar Pe for the weakly confined cell ($H = 30 \mu\text{m}$).

	$H = 30 \mu\text{m}$	$H = 10 \mu\text{m}$
Vortical flow speed, V ($\mu\text{m}^2/\text{s}$) (Figure 3A,C)	30	45 (also frontal flow)
Vortical diameter, l_V (μm) $2 \times$ vortex point distance (Figure 3B,D)	$2 \times 8.5 = 17$	$2 \times 20 = 40$
$t_{adv} = L/V$ (s)	0.57	0.8
$t_{diff} = L^2/D_S$ (s)	0.3	1.6
$Pe = t_{diff}/t_{adv}$	0.5	2

Appendix 1—table 1. Flow based Péclet number calculation from the flow fields in Figure 3.

1.4. Comparison of our experimental flow data in strong confinement with Liron & Mochon’s theoretical solution



Appendix 1—figure 1. Theoretically computed flow fields in confinement from Liron & Mochon’s formula. (A) Theoretically computed flow fields using Liron & Mochon’s solution for 2-Stokeslet model in 2D. The red arrows at $(6, \pm 11)$ μm denote the position of the Stokeslets. The colorbar represent flow magnitude normalised by its maximum, v_{nor} . Scalebar, 10 μm . (B) Comparison between normalised experimental flow of a cell swimming in $H = 10$ μm (Figure 3C) and Liron & Mochon’s theoretical flow field (A) along representative radial distances, r from the cell centre as a function of polar angle. Plots for each r are shifted along the y -axis for clarity. (C) Flow magnitude variation along 4 directions as indicated by separate colors in the *middle* inset [lateral to vortex (blue), lateral to cell centre (yellow), anterior (red), posterior (grey)] for the normalised experimental (symbols) and theoretical (solid lines) velocity fields in Figure 3C and Appendix 1—figure 1A, respectively. Except for the theoretical speed along the vortex direction (blue), others are negligible compared to the experiment as shown in the *rightmost* inset, which is a semilog plot of (C) in the y -axis.

The solution of Liron & Mochon for a parallel Stokeslet, \mathbf{F} between two plates is equivalent to that of a 2D source dipole of the form $v_i(r) \sim \left(-\frac{\delta_{ij}}{2r^2} + \frac{r_i r_j}{r^4} \right) F_j$ [40]. As we have explicitly shown that $|\mathbf{F}_{th}^{10}| \gg |\mathbf{F}_{cd}^{10}|$, the cell-body drag is insignificant and the observed flow field is mostly due to flagellar thrust. We, therefore, superpose Liron & Mochon’s solution for two flagellar forces and obtain the flow in Appendix 1—figure 1A. The streamlines of the ‘2-Stokeslet Liron & Mochon flow’ are qualitatively similar to that of the experiment

(Figure 3C). However, the 2-Stokeslet theoretical flow of Liron & Mochon decays much more rapidly than the experimental one and does not capture the experimental flow variation as shown in Appendix 1—figure 1B,C. Notably, there is no signature of vortex position lateral to the forcing point, i.e. no minimum in the blue solid curve in Appendix 1—figure 1C. Therefore, this theoretical model is insufficient to describe the flow variation, positions of vortices and other flow features of the strongly confined flow accurately. The root mean square deviation (RMSD) in v_x , v_y & $|\mathbf{v}|$ between the experimental flow of a H10 cell (Figure 3C) and 2-Stokeslet Liron & Mochon’s flow is 25.9%, 16.8% and 30.8%, respectively (see Materials and Methods for RMSD definition).

1.5. Inverse Fourier transform of the quasi-2D Brinkman equation in Fourier space

The quasi-2D Brinkman equation in Fourier space, Eq. (3) in the main text, is

$$\mathbf{v}_{\mathbf{k}} = \frac{\mathbf{O}_{\mathbf{k}} \cdot \mathbf{F}}{\eta \left(k^2 + \frac{\pi^2}{H^2} \right)} \quad (\text{A1})$$

Here, the orthogonal projection operator in polar coordinates (k, θ) is

$$\mathbf{O}_{\mathbf{k}} = 1 - \widehat{\mathbf{k}}\widehat{\mathbf{k}} = \begin{bmatrix} 1 - \widehat{k}_x^2 & -\widehat{k}_x\widehat{k}_y \\ -\widehat{k}_y\widehat{k}_x & 1 - \widehat{k}_y^2 \end{bmatrix} = \begin{bmatrix} \sin^2 \theta & -\sin \theta \cos \theta \\ -\sin \theta \cos \theta & \cos^2 \theta \end{bmatrix} \quad (\text{A2})$$

where θ is the angle between wave vector \mathbf{k} and x -axis. For Stokeslets/Gaussian forces pointing along x -direction only, as in our case, $\mathbf{F} = \begin{bmatrix} F \\ 0 \end{bmatrix}$, therefore $\mathbf{O}(\mathbf{k}) \cdot \mathbf{F} = \begin{bmatrix} \sin^2 \theta \\ -\sin \theta \cos \theta \end{bmatrix} F$.

To compute the velocity field in real space, we inverse Fourier transform Eq. (A1) in polar coordinates, by replacing the numerator as shown above

$$\mathbf{v}(\mathbf{r}) = \frac{1}{(2\pi)^2 \eta} \int e^{i\mathbf{k} \cdot \mathbf{r}} \begin{bmatrix} \sin^2 \theta \\ -\sin \theta \cos \theta \end{bmatrix} \frac{F k dk d\theta}{\left(k^2 + \frac{\pi^2}{H^2} \right)} \quad (\text{A3})$$

In polar coordinates, the field points in the $x-y$ plane are given by $(x, y) = (r \cos \phi, r \sin \phi)$, hence $\mathbf{k} \cdot \mathbf{r} = kr \cos(\theta - \phi)$. Thus, the fluid velocity field is

$$\begin{bmatrix} v_x \\ v_y \end{bmatrix} (r, \phi) = \frac{F}{4\pi^2 \eta} \int_0^{2\pi} d\theta \int_0^\infty dk \begin{bmatrix} \sin^2 \theta \\ -\sin \theta \cos \theta \end{bmatrix} \frac{k e^{i k r \cos(\theta - \phi)}}{\left(k^2 + \frac{\pi^2}{H^2} \right)} \quad (\text{A4})$$

Let us change the θ integral from $(0, 2\pi) \rightarrow (-\pi/2 + \phi, \pi/2 + \phi)$, where $\cos(\theta - \phi) > 0$. For example, the θ integral for v_x changes as follows,

$$\int_0^{2\pi} \sin^2 \theta e^{ikr \cos(\theta - \phi)} d\theta = \int_{-\pi/2 + \phi}^{\pi/2 + \phi} \sin^2 \theta e^{ikr \cos(\theta - \phi)} d\theta + \int_{\pi/2 + \phi}^{3\pi/2 + \phi} \sin^2 \theta e^{ikr \cos(\theta - \phi)} d\theta \quad (\text{A5})$$

Replacing $\theta \rightarrow \theta - \pi$ in the 2nd integral, the limits change as $(\pi/2 + \phi, 3\pi/2 + \phi) \rightarrow (-\pi/2 + \phi, \pi/2 + \phi)$, and the integrands $\sin \theta \rightarrow -\sin \theta$, $\cos \theta \rightarrow -\cos \theta$, $\cos(\theta - \phi) \rightarrow -\cos(\theta - \phi)$. Therefore, the 2nd integral in the above equation changes to $\int_{-\pi/2 + \phi}^{\pi/2 + \phi} \sin^2 \theta e^{-ikr \cos(\theta - \phi)} d\theta$.

Hence, v_x 's θ integral becomes

$$\int_0^{2\pi} \sin^2 \theta e^{ikr \cos(\theta - \phi)} d\theta = 2 \int_{-\pi/2 + \phi}^{\pi/2 + \phi} \sin^2 \theta \cos[kr \cos(\theta - \phi)] d\theta \quad (\text{A6})$$

Similarly, $\int_0^{2\pi} -\sin \theta \cos \theta e^{ikr \cos(\theta - \phi)} d\theta = 2 \int_{-\pi/2 + \phi}^{\pi/2 + \phi} -\sin \theta \cos \theta \cos[kr \cos(\theta - \phi)] d\theta$. Thus the velocity field in polar coordinates is given by,

$$\begin{bmatrix} v_x \\ v_y \end{bmatrix} (r, \phi) = \frac{F}{2\pi^2 \eta} \int_{-\pi/2 + \phi}^{\pi/2 + \phi} d\theta \int_0^\infty dk \begin{bmatrix} \sin^2 \theta \\ -\sin \theta \cos \theta \end{bmatrix} \frac{k \cos[kr \cos(\theta - \phi)]}{\left(k^2 + \frac{\pi^2}{H^2}\right)} \quad (\text{A7})$$

For Gaussian forces, the numerator just gets multiplied by $e^{-k^2 \sigma^2 / 2}$. We perform these 2D integrals in MATLAB for a 20×23 XY grid, with k integral ranging from 0 to 100 to obtain the theoretical flow fields in this article.

The above integration takes 3 hours of computational time for 2 Stokeslets whereas it takes only 1 minute to compute the flow field for 2 Gaussian forces of $\sigma = 5 \mu\text{m}$ (*Processor*: Intel i7-4770 CPU with clock speed 3.4 GHz). Hence, we try to write a semi-analytical expression for the case of 2 Stokeslets. Let us consider $kr \cos(\theta - \phi) = p$ and $\frac{\pi r \cos(\theta - \phi)}{H} = q$. Then the k -integral changes from $\int_0^\infty \frac{k \cos[kr \cos(\theta - \phi)]}{(k^2 + \pi^2/H^2)} dk \rightarrow \int_0^\infty \frac{p \cos p}{p^2 + q^2} dp$. We rename this integral as $I(q)$ and calculate it using the Exponential Integral, Ei (Eq. 3.723–5 of [59]).

$$I(q) = \int_0^\infty \frac{p \cos p}{p^2 + q^2} dp = -\frac{1}{2} [e^{-q} \overline{\text{Ei}}(q) + e^q \text{Ei}(-q)] \quad (\text{A8})$$

where,

$$\text{Ei}(q) = -\int_{-q}^\infty \frac{e^{-m}}{m} dm = \int_{-\infty}^q \frac{e^m}{m} dm, \quad \text{for } q < 0 \quad (\text{A9})$$

and to avoid the singularity for $q > 0$, it is defined by using the principal value of the integral as

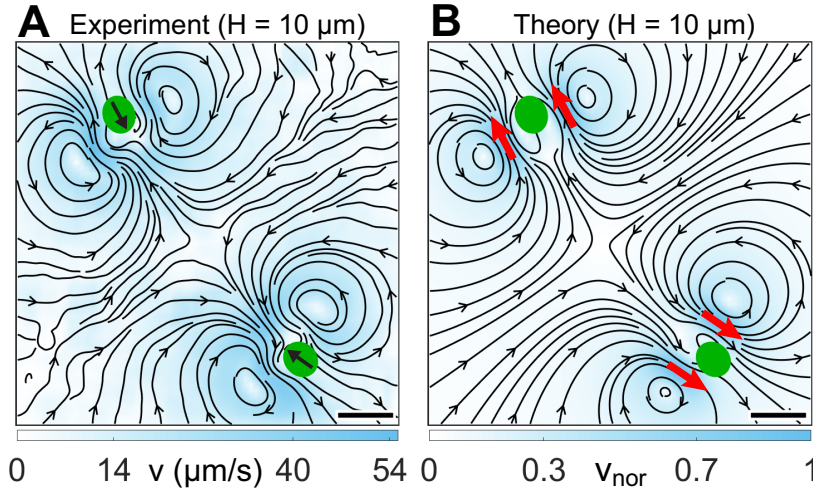
$$\overline{\text{Ei}}(q) = \int_{-\infty}^{-\epsilon} \frac{e^m}{m} dm + \int_{\epsilon}^q \frac{e^m}{m} dm, \quad \text{where } \epsilon > 0, \quad \text{for } q > 0 \quad (\text{A10})$$

In our case $q > 0$, so we use Eq. (A9) for calculating $\text{Ei}(-q)$ and Eq. (A10) for calculating $\overline{\text{Ei}}(q)$, wherein we use $\epsilon = 10^{-5}$. So, Eq. (A7) reduces to

$$\begin{bmatrix} v_x \\ v_y \end{bmatrix} (r, \phi) = \frac{F}{2\pi^2\eta} \int_{-\frac{\pi}{2}+\phi}^{\frac{\pi}{2}+\phi} d\theta \begin{bmatrix} \sin^2 \theta \\ -\sin \theta \cos \theta \end{bmatrix} I(q) \quad (\text{A11})$$

This method computes the flow field for 2 Stokeslets in 12 minutes.

1.6. Is the 2-Gaussian Brinkman model applicable to a collection of strongly confined pullers?



Appendix 1—figure 2. Flow fields due to two strongly confined H10 cells. (A) Experimentally measured flow field for two synchronous cells swimming in $H = 10 \mu\text{m}$. This flow is averaged over ~ 30 beat cycles for each cell during which the cells move merely 0.05 times their respective body diameters ($D \sim 12.42 \mu\text{m}$). The centre-to-centre distance between the swimmers is $8.75D$. Black arrows on the cell bodies indicate their swimming direction. Solid black lines indicate the streamlines of the flow in lab frame. The colorbar represents flow magnitude, v . (B) Theoretically computed flow field by linearly superposing two 2-Gaussian Brinkman flow, one for each cell. The position of the pair of 2-Gaussian forces at approximate flagellar positions are denoted by red arrows. The streamlines, vortex flows and stagnation point at the centre of the grid match qualitatively with the experimental one (A). The colorbars represent flow magnitudes normalised by their maximum, v_{nor} . Scalebar, $20 \mu\text{m}$.

We analyse the fluid flow due to two strongly confined H10 Synchronous cells as a preliminary test for determining the applicability of our theoretical methodology to a collection of

microswimmers. Specifically, we measure the beat averaged flow field of two synchronously beating cells which are separated by ~ 9 body diameters and approach each other head-on ([Appendix 1—figure 2A](#)). Therefore, we linearly superpose the solution of the quasi-2D Brinkman equation for a pair of 2-Gaussian forces ($\sigma = 5 \mu\text{m}$) at the approximate flagellar positions of the two cells and obtain the resultant flow field ([Appendix 1—figure 2B](#)). The position and direction of flow vortices along with the stagnation point in between the two cells match well between the experiment and theory. This suggests that linearly superposing 2-Gaussian Brinkman flows might be an adequate description for the flow field of a dilute collection of CRs.